79-4033

Transonic Flows Past Nonaxisymmetric Slender Shapes—Classical Equivalence Rule Analysis

Stephen S. Stahara*
Nielsen Engineering & Research, Inc., Mountain View, Calif.
and
John R. Spreiter†
Stanford University, Stanford, Calif.

An assessment of the classical transonic equivalence rule is provided. Extensive comparisons of theoretical results are made with data obtained in conventional transonic tunnels for various slender bodies, as well as a thin triangular wing of unit order aspect ratio. Results are reported for surface and flowfield pressure distributions at Mach numbers throughout and beyond the transonic range for both nonlifting and lifting conditions. Particular attention has been paid to wind tunnel interference effects through use of an interesting alternative to the classical homogeneous wall condition, whereby experimentally measured flowfield pressures are imposed as an outer boundary condition. The comparisons with experiment display good agreement, including the region near shock waves, and indicate that the classical equivalence rule approximation remains effective for certain three-dimensional aerodynamic configurations over a broad range of geometries and flow conditions.

Introduction

THE purpose of this paper is to present an assessment, based on recent extensive theoretical comparisons with data, of the transonic equivalence rule. Attention is focused primarily on high supercritical and low supersonic flows past a number of three-dimensional slender aerodynamic shapes having low-to-moderate lift. The analysis centers on the small-disturbance theory of steady inviscid transonic flows, and employs the classical thickness-dominated form of the transonic equivalence rule. Use is made of analytic slender-body crossflow solutions for the inner region, and finite-difference successive line over-relaxation (SLOR) solutions of the axisymmetric transonic small-disturbance equation for the outer region. Special emphasis is directed toward wind tunnel wall interference effects.

Results are presented for pressure distributions on the surface and in the near flowfield of a variety of slender configurations, for both nonlifting and lifting conditions, at Mach numbers within and beyond the transonic regime. The shapes considered are slender parabolic-arc bodies having various elliptic cross sections and a thin low aspect-ratio triangular wing with elliptic cross section. Angles of attack range from 0 to 6 deg. The particular configurations and flow conditions were purposely selected to enable comparison with existing data obtained in conventional transonic wind tunnels.

The analysis employed, and the subsequent theoretical results, provide the proper comparative basis with which to judge the classical equivalence rule with experiment. Thus, the previous results given in Ref. 1, which heretofore provided the most extensive comparison of the classical equivalence rule with experiment, have been extended in several important directions. Freestream Mach numbers have been considered from 0.90 to 1.20, as well as at $M_\infty = 1.00$, with emphasis on situations where embedded shock waves are located on the body surface and bow shocks are unattached. Additionally, actual sting geometry is accounted for, and corrections for wind-tunnel wall interference effects are included in all of the theoretical results presented.

Received April 27, 1978; revision received Nov. 7, 1978.

Index categories: Transonic Flow; Computational Methods.

*Senior Research Scientist. Member AIAA.

†Professor, Division of Applied Mechanics; consultant, Nielsen Engineering & Research, Inc. Fellow AIAA.

Analysis

Basic Equations and Boundary Conditions

The coordinate system employed in the analysis is a body-fixed Cartesian system with origin at the nose of the configuration, and orientation such that the x axis is directed downstream and coincident with the longitudinal body axis, the y axis to the right facing forward, and the z axis directed vertically upward, as illustrated in Fig. 1. The oncoming freestream may be inclined in pitch to the x axis at some arbitrary small angle α, but sideslip has not been considered. The flow is assumed to be inviscid and steady, and the configurations sufficiently slender and smooth that the resulting flowfield is irrotational and adequately treated by small-disturbance theory. Accordingly, a disturbance velocity potential ϕ can be defined by[2]:

$$\Phi(x,y,z) = U_\infty \ell \, [x + \alpha z + \phi(x,y,z)] \tag{1}$$

where Φ is the total velocity potential, U_∞ represents the freestream velocity, ℓ is the body length, and the coordinates (x,y,z) have been nondimensionalized by ℓ. The governing partial differential equation for ϕ, appropriate for the low-lifting slender configurations considered, is given by:

$$(1-M_\infty^2)\phi_{xx} + \phi_{yy} + \phi_{zz} = \frac{\partial}{\partial x}\left[\frac{1}{2} M_\infty^2 (\gamma+1)\phi_x^2\right] \tag{2}$$

We note that the quadratic terms $(\phi_y^2 + \phi_z^2)$, which usually appear[3,4] within the bracket on the right-hand side to account for situations where the lift is significant, are of higher order and negligible for thickness-dominated situations. For the body-fixed coordinate system shown in Fig. 1, the expression for the pressure coefficient is given by:

$$C_p = \frac{p - p_\infty}{\rho_\infty U_\infty^2/2} = -2(\phi_x + \alpha\phi_z) - (\phi_y^2 + \phi_z^2) \tag{3}$$

In general, the boundary conditions to be satisfied consist of: 1) far-field conditions appropriate to the behavior of the flow far from the body in either a free-air flow or in a wind tunnel

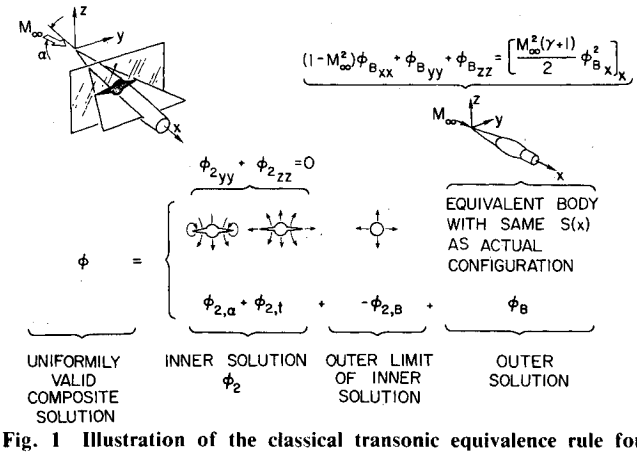

Fig. 1 Illustration of the classical transonic equivalence rule for slender configurations.

environment; 2) the body surface condition that the velocity component normal to the body surface be zero at the body; and 3) shock wave conditions to be applied at any shock surface appearing in the flow, such that the potential is continuous through the shock and the velocity components satisfy the small-disturbance approximation to the Rankine-Hugoniot conditions at the location of the shock. These requirements lead for slender shapes to the following conditions on ϕ for free air flows:

$$\phi(\infty)=0 \tag{4}$$

$$[(n_1+\alpha n_3)+n_2\phi_y+n_3\phi_z]_{\text{body}}=[(n_1+\alpha n_3)+\phi_n]_{\text{body}}=0 \tag{5}$$

$$[\![\,\phi]\!]_{\text{shock}}=0,\quad [\{(1-M_\infty^2)-M_\infty^2(\gamma+1)\langle\phi_x\rangle\}[\![\,\phi_x^2]\!] + [\![\,\phi_y^2]\!]+[\![\,\phi_z^2]\!]]_{\text{shock}}=0 \tag{6}$$

where $\hat{n}=\hat{i}n_1+\hat{j}n_2+\hat{k}n_3$ is the unit normal to the body surface, (n_1,n_2,n_3) are the direction cosines of $\hat{n}$ with respect to the (x, y, z) axes, and the symbols $[\![\ ]\!]$ and $\langle\rangle$ signify the difference and the mean, respectively, of the enclosed quantity on the two sides of the shock surface. For flows in a wind tunnel environment, the appropriate condition employed to replace Eq. (4) is detailed in a subsequent section discussing the outer flow solution.

Transonic Equivalence Rule for Thickness-Dominated Flows

The transonic equivalence rule (TER) was developed initially in the form, now known as the classical or thickness-dominated limit, by Oswatitsch[5,6] for thin nonlifting wings, and extended later to moderately lifting wings[7] and slender configurations of arbitrary cross section.[2] Subsequent extensions of the rule[3,4,8] to include situations where the lift is significant both revealed its dependence on lift as well as clarified the classical limit and range of validity. In essence, the rule provides the basis for greatly simplifying the calculation of transonic flows past a special but aerodynamically important class of three-dimensional configurations. It accomplishes this by recognizing that the structure of transonic flows past slender shapes in the vicinity of $M_\infty \approx 1$ consists of two distinct but coupled domains whose governing equations and boundary conditions are significantly easier to solve than the original equations, Eqs. (2 and 4-6). The fundamental structure of the equivalence rule is found to be governed principally by a parameter σ_* (Ref. 4) involving a combination of the configuration thickness ratio, lift force, and leading-edge sweep, and which represents essentially the ratio of lift/thickness effects. Depending on the magnitude of σ_*, the nonlinear outer problem can be classified into one of three domains: 1) $\sigma_* \ll 1$, thickness-dominated, 2) $\sigma_* = 0(1)$, intermediate, and 3) $\sigma_* \gg 1$, lift-dominated. For the classical TER, which represents the first-order (in σ_*) thickness-dominated limit, the solution domains consist of an inner region governed by a linear equation, the same as in slender-body theory, and an outer nonlinear region consisting of the axisymmetric flow about an "equivalent" nonlifting body of revolution having the same longitudinal distribution of cross-sectional area.

The theoretical essentials of the equivalence rule for thickness-dominated flows are illustrated in Fig. 1, which displays the decomposition of the flow into its first-order inner and outer components, and the resulting uniformly valid composite solution; that is,

$$\phi=\phi_{2,\alpha}+\phi_{2,t}-\phi_{2,B}+\phi_B \tag{7}$$

Here, each component of ϕ has the meaning indicated in Fig. 1. The first-order lift ($\phi_{2,\alpha}$) and thickness ($\phi_{2,t}$) inner solutions describe, respectively, the translating and expanding cross section in the y,z plane, and satisfy the two-dimensional Laplace equation:

$$\phi_{2yy}+\phi_{2zz}=0 \tag{8}$$

together with the no-flow boundary condition at the body surface in the y,z plane at each x station. The first-order outer solution ϕ_B satisfies the axisymmetric transonic small-disturbance equation:

$$(1-M_\infty^2)(\phi_B)_{xx}+(\phi_B)_{rr}+(1/r)(\phi_B)_r = [\tfrac{1}{2}M_\infty^2(\gamma+1)(\phi_B)_x^2]_x \tag{9}$$

subject to an inner boundary condition determined by the "equivalent" body singularity source distribution. This, in turn, is determined by the outer behavior ($\phi_{2,B}$) of the inner solution:

$$\lim_{r\to 0}(r(\phi_B)_r)=\lim_{r\to\infty} r\{\phi_{2,\alpha}+\phi_{2,t}\}_r = r(\phi_{2,B})_r = S'(x)/2\pi \tag{10}$$

where $S(x)$ is the equivalent body cross-sectional area nondimensionalized by ℓ^2, and the effect of lift is recognized to be small in comparison to thickness effects, so that its contribution to the outer flow is of a higher order in σ_*. Shock conditions appropriate to the outer flow are given by:

$$[\![\,\phi_B]\!]_{\text{shock}}=0,\quad [r\{1-M_\infty^2-M_\infty^2(\gamma+1)\langle\phi_{Bx}\rangle\}[\![\,\phi_{B_x}^2]\!] + [\![\,(r\phi_{B_r})^2]\!]]_{\text{shock}}=0 \tag{11}$$

The final boundary condition for the outer problem relates to conditions representative of the flow far from the configuration. For free air this is given by Eq. (4), while appropriate conditions for a tunnel environment are discussed in the following section.

Higher order TER solutions for thickness-dominated flows beyond the first-order terms indicated in Eqs. (7-11) can be determined systematically by the methods described in Refs. 3 and 4. These consist of a doubly infinite coupled series of inner and outer solutions. In general, the higher order inner solutions satisfy a Poisson equation in the crossflow plane, with the right-hand side a known function of lower order inner solutions; while the higher order outer solutions satisfy a linear equation with nonconstant coefficients dependent on the first-order outer (ϕ_B) solution. For the results presented here, only the first-order components are employed.

Outer Flow Solution

The method employed to determine the outer flow component ϕ_B satisfying Eqs. (9-11) is a finite-difference SLOR

procedure using Murman-Cole type-dependent difference operators.[9-11] To implement the calculation, we have employed the following fully conservative form of Eq. (9):

$$[\eta(K\bar{\phi}_x - \tfrac{1}{2}\bar{\phi}_x^2)]_x + [\eta\bar{\phi}_\eta]_\eta = 0 \tag{12}$$

where

$$\bar{\phi}(x,\eta) = (1/\tau^2)\phi_B(x,r), \quad K = (1-M_\infty^2)/(\tau^2 M_\infty^2)(\gamma+1)$$

$$\eta = \tau M_\infty \sqrt{\gamma+1}\, r \tag{13}$$

and τ signifies the thickness ratio of the equivalent body. Additionally, the actual finite-difference form of the equation used is that suggested by Jameson[15] and a pseudo-time term of the form $\epsilon\phi_{B_{xt}}$ was added to enhance stability and speed convergence. The inner boundary condition, Eq. (10), becomes

$$\lim_{\eta\to 0}(\eta\bar{\phi}\eta) = \frac{\bar{S}'(x)}{2\pi} \tag{14}$$

where $\bar{S}(x) = S(x)/\tau^2$. Since all the comparative experimental data used in this study were obtained in conventional transonic wind tunnels,[12,13] an appropriate outer boundary condition to replace the free air condition at infinity [Eq. (4)] is required. One choice is the classical homogeneous wall boundary condition which, for the data considered here, is the porous condition:

$$\bar{\phi}_\eta + \bar{P}\bar{\phi}_x = 0 \tag{15}$$

where $\bar{P} = P/\tau M_\infty\sqrt{\gamma+1}$ is the transonically scaled porosity. Although such a wall condition is useful for obtaining overall trends, as Bailey[9] and others have demonstrated, the inadequacies of the approximation are well known. In the results reported herein, we have used an interesting and more accurate alternative, which is described in Ref. 14. The procedure consists of employing a single experimentally measured flow parameter—in our case the pressure—along a cylindrical control surface located sufficiently inward from the actual tunnel walls so as to be removed from the local wall disturbances. The boundary condition imposed on $\bar{\phi}$ is of Dirichlet-type and is given by:

$$\bar{\phi}(x,\eta_s) = \frac{-1}{2\tau^2}\int_{x_1}^{x} C_{p_m}(\xi,\eta_s)\,d\xi \tag{16}$$

where $\eta_s = \tau M_\infty\sqrt{\gamma+1}\, r_s$ denotes the transonically scaled radial location of the control surface, x_1 the position of the upstream boundary, C_{p_m} the measured pressure coefficient, and $\bar{\phi}(x_1,\eta_s)$ has been set to zero for convenience. Further details and an evaluation of the procedure are provided in Ref. 14.

Results

Surface and Flowfield Pressure Distributions on Several Nonlifting Bodies

To provide both a comparative basis with experiment, as well as determine the nonlinear equivalent body solutions for the nonaxisymmetric shape to follow, we have prepared Fig. 2. This figure displays a comparison of theoretical results with data[12] for a parabolic-arc body of revolution having a diameter to complete body length $D/\ell = 1/12$. Results are shown at freestream Mach numbers $M_\infty = 0.975$, 1.00, 1.025, and 1.10. The data were obtained in the Ames 14-ft wind tunnel where, for the body tested, the tunnel half-height to body length ratio was $H/\ell = 7/6$. The theoretical results are indicated by solid lines and represent the SLOR solutions of Eqs. (12-14). For the results shown in Fig. 2, the measured pressure distribution outer condition, Eq. (16), was employed. Pressure survey data obtained at the radial location $r/D = 4$ were used, which represented the outermost survey at which data were taken.

The theoretical body surface pressure coefficients were determined by extrapolating the SLOR results obtained along the first radial grid line r_1 down to the body surface according to the slender body result

$$C_p(x,R) = -\left[2\phi_x(x,r_1) + \frac{S''(x)}{\pi}\ell n\left(\frac{R}{r_1}\right) + \left(\frac{dR}{dx}\right)^2\right] \tag{17}$$

where R is the equivalent body radius. The flowfield pressures were calculated by bilinear interpolation for ϕ through the flowfield grid; and then employing the formula

$$C_p(x,r) = -2\phi_x(x,r) - \phi_r^2(x,r) \tag{18}$$

The (x,r) mesh density used for these results was 80×24 with 40 equally spaced points on the body. The r grid as well as the x grid ahead and behind the body were expanded geometrically using a grid ratio of 1.2:1. The x mesh extended two body lengths ahead and three body lengths behind the body, and the location of the first r grid line was at $r = \tau/2$. Relaxation factors $1.7 < \omega < 1.9$ were used and the coefficient of the pseudo-time term was set to $\epsilon = 0.5$. Convergence in all cases was very rapid, with a $|\Delta\phi|_{\max} < 10^{-5}$ criteria reached within 75 iteration sweeps. Pressure changes on the body usually became less than 10^{-4} before 40 iterations.

With regard to the comparisons, we note that the agreement of the theoretical results with data for both surface and flowfield pressure is excellent. The numerical procedure is able to predict with accuracy and throughout the Mach

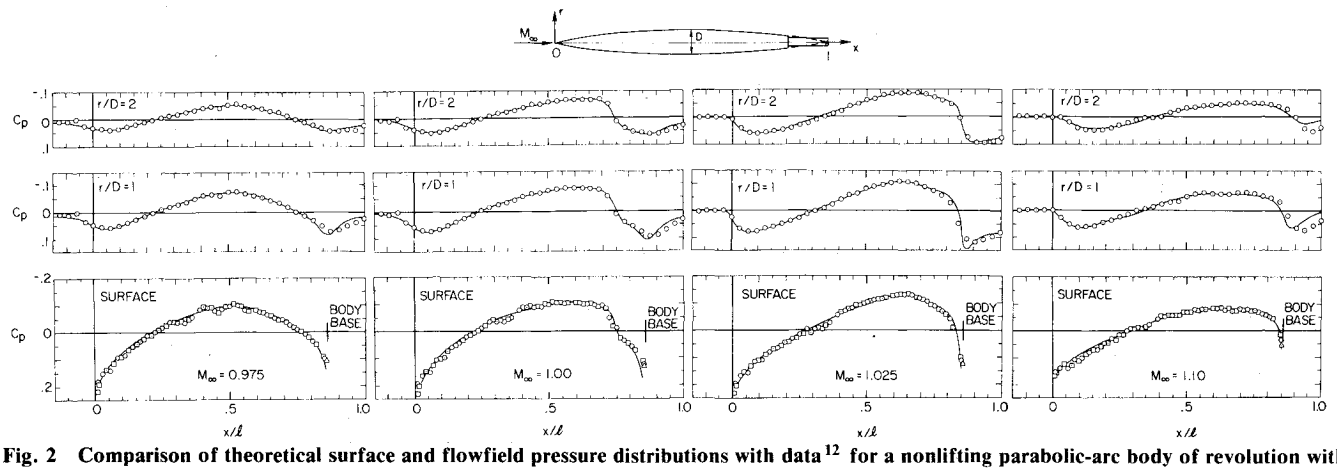

Fig. 2 Comparison of theoretical surface and flowfield pressure distributions with data[12] for a nonlifting parabolic-arc body of revolution with thickness ratio $D/\ell = 1/12$ at several transonic Mach numbers.

number range the location and strengths of both surface and bow shocks. Wind tunnel interference effects, known to be significant for this shape,[14] are properly accounted for via the outer boundary condition, and the actual sting geometry has been included.

A further point regarding the comparisons in the vicinity of the shock is noteworthy. This relates to the fact that presumably an exact solution of the transonic small-disturbances in the vicinity of the shock would, in the limit of vanishing grid spacing, yield a sharp discontinuity, as well as a singularity, at the foot of the shock. This is unlike the rather smooth transition indicated by the data, which are presumably softened by shock-boundary-layer interaction. Therefore, the apparent agreement of the numerical solution with data near the shock would appear to be fortuitous. We have examined this point further for the $M_\infty = 1.00$ case shown in Fig. 2 by obtaining numerical solutions employing a very fine grid ($\Delta x/\ell = 0.004$) in the vicinity of the shock. It was observed that while a sharp shock discontinuity is obtained with the fine grid, no postshock expansion, as is common in two-dimensional results, is found; the flow continued to decelerate smoothly beyond the foot of the shock. Moreover, the character of the fine grid pressure distribution in the shock region was found to be quite close to the calculated coarse grid results displayed in Fig. 2.

The point of dwelling on these comparisons is to establish the accuracy of the equivalent body solutions which form the basis of the TER calculations to follow. In the previous work,[1] it was recognized that one cause of the discrepancies observed in the TER comparisons with data[12] were due to deficiencies in the equivalent body solution. The extent of those discrepancies could only be conjectured, since an accurate equivalent body solution procedure was unavailable at that time. The importance of this for the results to follow is that those solutions presented are essentially exact solutions of the TER theoretical model given by Eqs. (7-11).

As a first application of the TER combined with finite-difference results for the axisymmetric flow past the equivalent body of revolution, we have considered a family of slender bodies with elliptic cross sections which were tested in the Ames 14-ft transonic wind tunnel.[12] Figure 3 presents the nonlifting pressure distributions measured along the extremities of the major and minor axes ($\theta = 0$, 90 deg) at $M_\infty = 0.975$ and 1.025 for three of these bodies having values for the ratio $\lambda = a/b$ of major to minor axes of the elliptical cross section of 1.5, 2.0, and 3.0. These bodies were constructed so that the ratio of major to minor axes remains constant along the length of the body. Furthermore, all the bodies have the identical longitudinal distribution of cross-sectional area $S = \pi ab$ as the parabolic-arc body of revolution with $D/\ell = 1/12$ for which results were shown in Fig. 2. In determining the theoretical results, the following expressions for $\phi_{2,I}$ and $\phi_{2,B}$ apply[1]:

$$\phi_{2,I} = \text{R.P.}\left\{\frac{S'(x)}{2\pi}\ln\left[\frac{\sigma + (\sigma^2 - a^2 + b^2)^{1/2}}{2}\right]\right\} \tag{19}$$

$$\phi_{2,B} = \frac{S'(x)}{2\pi}\ln r \tag{20}$$

where R.P. signifies the real part of the complex quantity contained within the brackets and $\sigma = y + iz = re^{i\theta}$. Solutions required for the equivalent body potential ϕ_B for use in Eq. (7) were determined previously from Eqs. (12-16) in arriving at the results in Fig. 2, and C_p is related to ϕ by Eq. (3) with $\alpha = 0$.

With regard to the comparisons displayed in Fig. 3, the theoretical and experimental results are in good agreement along the entire body length at both Mach numbers and for all three bodies. In particular, the comparisons are not deficient

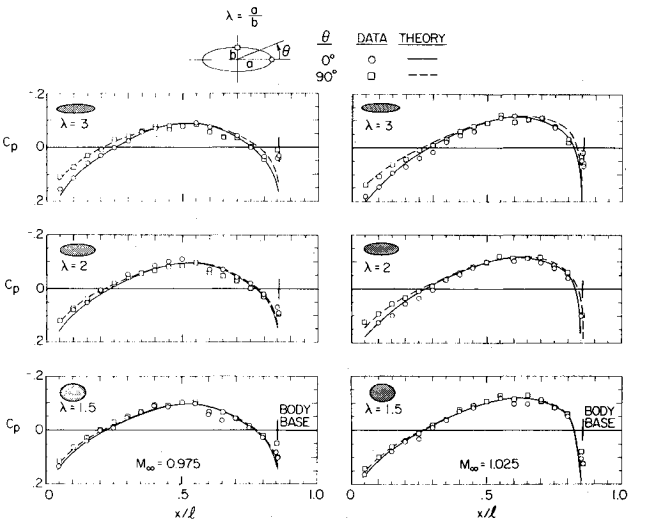

Fig. 3 Comparison of TER results with experiment[12] for surface pressure distributions along the major and minor axes ($\theta = 0$, 90 deg) of three nonlifting slender bodies with different elliptic cross sections.

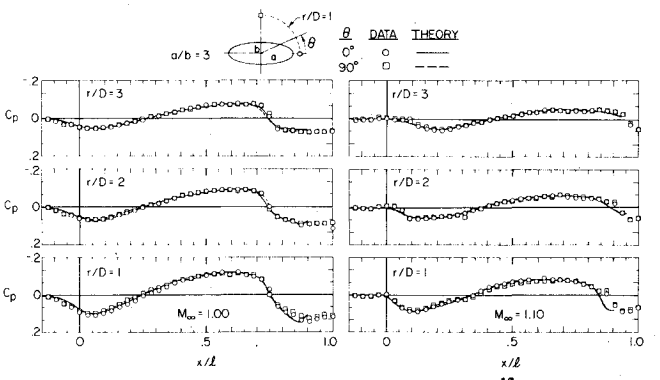

Fig. 4 Comparison of TER results with experiment[12] for flowfield pressure distributions for a nonlifting body having elliptic cross section with $a/b = 3$.

near the body base as before,[1] but are very satisfactory. The most notable feature of these results is the smallness of the effects of ellipticity of the cross section. Comparison with the corresponding results for the equivalent body shown in Fig. 2 indicates the relatively slight effect that the modified cross section has even for the most elliptic shape with $\lambda = 3$.

Analogous results for the flowfield at $M_\infty = 1.00$ and 1.10 are shown in Fig. 4 for the body having $\lambda = 3$. As could be expected from the surface pressure results of Fig. 3, theflowfield pressures also exhibit a strong tendency to become axisymmetric. The results indicated for this most strongly nonaxisymmetric shape are virtually independent of the azimuthal angle θ, and are essentially identical to those for the equivalent body shown in Fig. 2. Again, the TER results are in excellent agreement with the data.

Surface Pressure Distributions on Lifting Bodies

For the initial application of the TER to lifting flows, we have considered the flow at $M_\infty = 1.00$ past the parabolic-arc body of revolution with $D/\ell = 1/12$, for which results at zero angle of attack were provided in Fig. 2. Figure 5 displays the comparison between the TER results and data obtained in the Ames 14-ft transonic wind tunnel[12] at angles of attack $\alpha = 2$, 4, and 6 deg along the five lines on the surface of the body given by $\theta = \pm 90$, ± 40, and 0 deg. For the theoretical results, the crossflow lifting potential $\phi_{2,\alpha}$ for use in Eq. (7) is given by:

$$\phi_{2,\alpha} = \alpha S(x)\sin\theta/\pi r \tag{21}$$

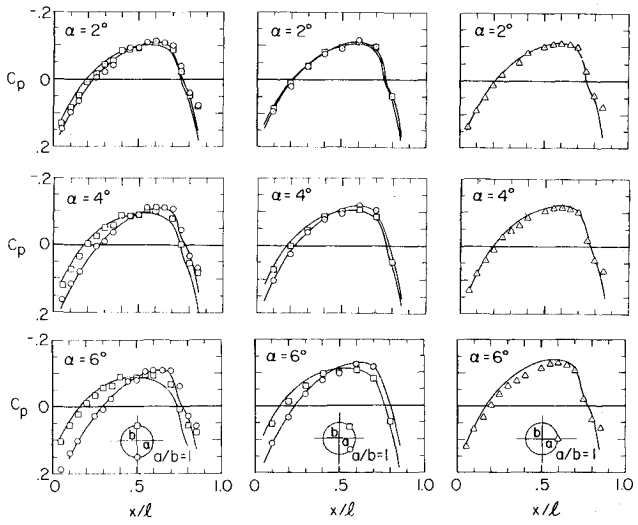

Fig. 5 Experimental[12] and TER results for surface pressure distributions at $M_\infty = 1.00$ along the lines $\theta = (\pm 90$ deg □, ± 40 deg ○, 0 deg △) on a lifting parabolic-arc body at three angles of attack.

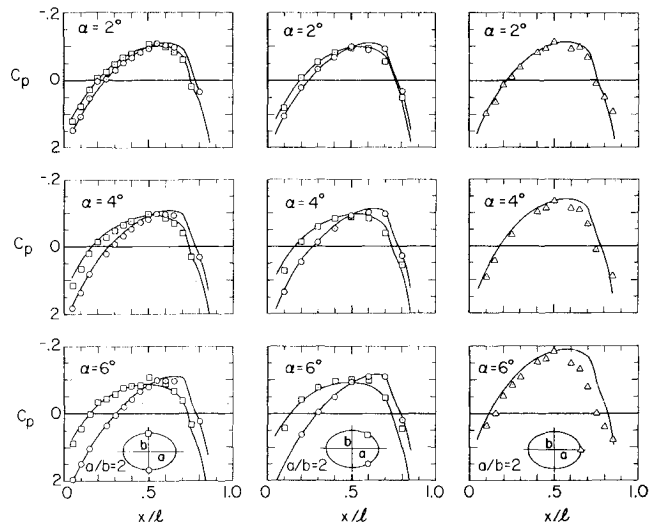

Fig. 6 Experimental[12] and TER results for surface pressure distributions at $M_\infty = 1.00$ along the lines $\theta = (\pm 90$ deg □, ± 40 deg ○, 0 deg △) on a lifting body having elliptic cross section with $a/b = 2$ at three angles of attack.

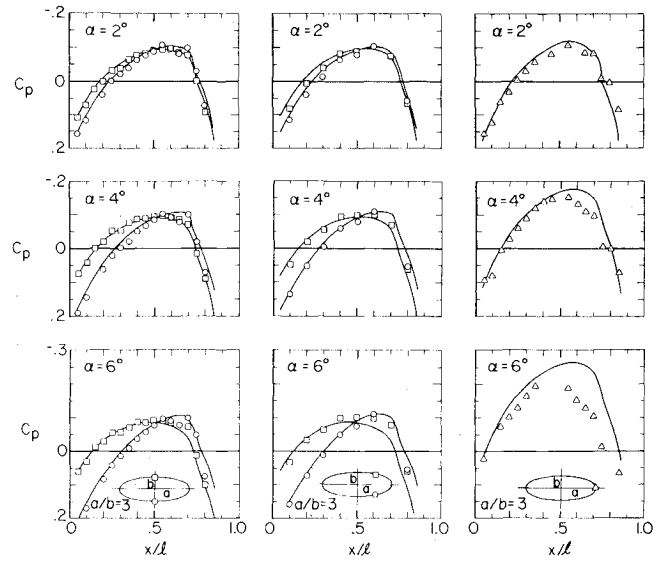

Fig. 7 Experimental[12] and TER results for surface pressure distributions at $M_\infty = 1.00$ along the lines $\theta = (\pm 90$ deg □, ± 40 deg ○, 0 deg △) on a lifting body having elliptic cross section with $a/b = 3$ at three angles of attack.

while $\phi_{2,l} = \phi_{2,B}$, where $\phi_{2,B}$ is given by Eq. (20), ϕ_B represents the same equivalent body solution of Eqs. (12-16) for which results were given previously in Fig. 2, C_p is given by Eq. (3), and ϕ by Eq. (7). In contrast to the nonlifting flow results shown in Figs. 2-4, these results display a significant dependence on azimuthal angle. Additionally, a strong variation with angle of attack is also evident. We observe that TER results are in good agreement with the data along the entire body length for all three angles of attack and, in particular, in the vicinity of the shock and the body base. The agreement in the vicinity of the shock is noteworthy and deserves further comment. Since within the accuracy of the classical TER theory, the longitudinal locations of any shock waves on the equivalent body are similarly located at the same longitudinal station on the actual slender configuration, at first glance it would appear that the classical equivalence rule would be significantly inaccurate in the vicinity of any shock surfaces due to three-dimensional displacement effects. This might be the situation if the shocks were sharp compressions, as is more frequently the case for two-dimensional transonic flows. However, for the axisymmetric and three-dimensional flows shown here, the experimental and theoretical pressure results for both surface and flowfield indicate compressions which are more gradual. This is due to a special characteristic of flows past these shapes, whereby the expansion waves originating from the forepart of the body are reflected from the sonic surface as compression waves and subsequently focused onto the aft portion of the body. This focusing effect produces an active mechanism for smoothly decelerating the flow in the region where the shock wave will form, and effectively results in a smearing of the shock and a subsequent flow situation which is more amenable to treatment by the classical TER. Consequently, for certain classes of slender configurations, the classical TER is capable of providing an accurate approximation for the flowfield properties even in the vicinity of shock waves.

Additional comparisons of TER results and data[12] for lifting flows are shown in Figs. 6 and 7. These results are for the bodies having elliptic cross section with ratio of major to minor axes $a/b = 2$ and 3 for which nonlifting results were given in Fig. 3. The expression for the crossflow lifting potential $\phi_{2,\alpha}$ required is given by:

$$\phi_{2,\alpha} = \text{R.P.}\left\{\frac{i\alpha}{2}\left[\sigma - (\sigma^2 - a^2 + b^2)^{1/2} + \frac{(a+b)^2}{\sigma + (\sigma^2 - a^2 + b^2)^{1/2}}\right]\right\} \tag{22}$$

and represents the two-dimensional potential flow about a body of elliptic cross section translating downward through still air with uniform velocity α.[16] The comparisons shown in Fig. 6 for the body with $a/b = 2$ display the same general good agreement observed for the body of revolution with one exception. This concerns the comparisons indicated by the three plots on the right side of the figure, which exhibit the pressure distributions along the major axis $\theta = 0$ deg as a function of angle of attack. The discrepancies observed between data and theory as α is increased to 6 deg, and which are not evident at the other azimuthal locations $\theta = \pm 90$, ± 40 deg, lead us to conjecture that the data are being influenced by vortex separation due to the crossflow velocity component, a result familiar at subsonic and supersonic speeds as well. The analogous comparisons shown in Fig. 7 for the body with $a/b = 3$ reinforces this observation. As before, the discrepancies at $\theta = 0$ deg are most pronounced at $\alpha = 6$ deg and have moved further forward than on the $a/b = 2$ body, a result which would be anticipated from body vortex separation phenomena.

While all the results shown in Figs. 5-7 were purposely calculated at $M_\infty = 1.00$, to provide both a severe test of the method and some benchmark comparisons with previous

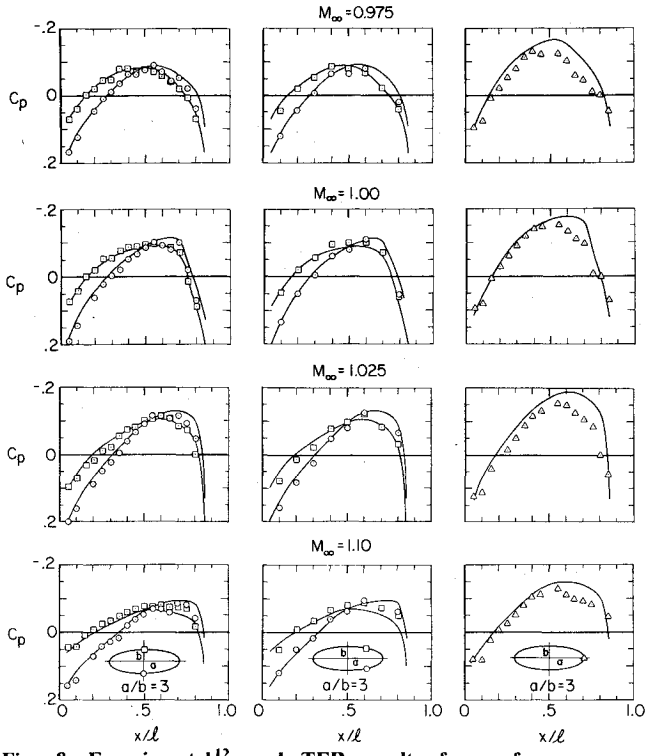

Fig. 8 Experimental[12] and TER results for surface pressure distributions at along the lines $\theta = (\pm 90$ deg □, ± 40 deg ○, 0 deg △) on a lifting body having elliptic cross section with $a/b = 3$ at $\alpha = 4$ deg and four transonic Mach numbers.

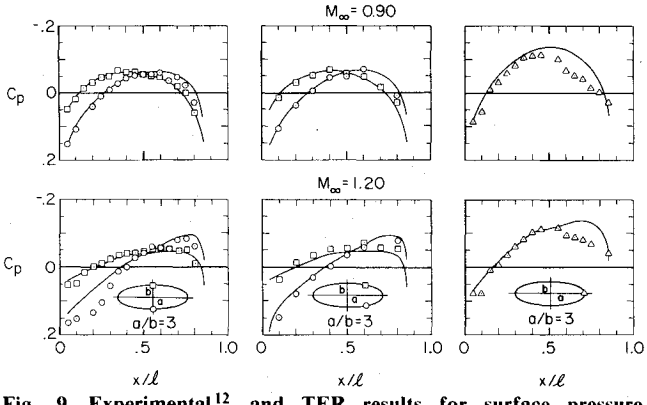

Fig. 9 Experimental[12] and TER results for surface pressure distributions along the lines $\theta = (\pm 90$ deg □, ± 40 deg ○, 0 deg △) on a lifting body having elliptic cross section with $a/b = 3$ at $\alpha = 4$ deg and $M_\infty = 0.90$ and 1.20.

results,[1] the question arises whether the TER results deteriorate as the freestream Mach number moves away from 1. Toward this end, we have tested the TER method at Mach numbers throughout the transonic regime against data for all three of the shapes considered in Figs. 5-7. Results for the most elliptic body with $a/b = 3$ are shown in Fig. 8, which displays a comparison of lifting surface pressure distributions at $M_\infty = 0.975$, 1.00, 1.025, and 1.10 and $\alpha = 4$ deg. With the exception of the discrepancy along the major axis ($\theta = 0$ deg) which was noted previously, the agreement of the classical TER results with the data is good throughout the entire transonic range. The large change in the character of the pressure distributions as the flow proceeds from $M_\infty = 0.975$ to 1.10 is well predicted by the theoretical method. Since this shape is the most severe geometrically, and because the results indicated in Fig. 8 are typical of the other shapes, for brevity the corresponding results for the bodies with $a/b = 1$ and 2 have been omitted. As a final comparison for this class of shapes, we have prepared Fig. 9, which exhibits similar comparisons to those of Fig. 8 but at Mach numbers well outside the transonic regime for slender bodies; that is, $M_\infty = 0.90$ and 1.20. Once again, the comparisons are quite good, indicating that for certain slender configurations, the equivalence rule remains valid over a surprisingly broad range of Mach numbers.

Pressure Distributions on Thin Wings

As a final application of the classical TER method, we have considered a thin triangular wing having elliptic cross section such that the equivalent body of revolution is a slender cone. These shapes were first considered theoretically in Ref. 2 and experimentally in Ref. 13 for a triangular wing having a leading-edge sweep angle of 45 deg, an aspect ratio of 2, and a thickness ratio of 0.06. These parameters for the wing lead to a ratio of major to minor axis of the elliptic cross section of $a/b = 16.67$. The corresponding equivalent body, which is a cone, has a semiapex angle equal to 0.1225 rad or 7 deg. For determining $\phi_{2,\alpha}$ and $\phi_{2,t}$ for the wing, either Eqs. (19) and (22) can be used directly or, alternatively, the simplified expressions which result when $a/b \gg 1$,

$$\phi_{2,t} = (ta/2\ell)\ell n(a/2) \quad \phi_{2,\alpha} = \pm\alpha(a^2 - y^2)^{1/2} \tag{23}$$

In Eq. (23), $\phi_{2,t}$ and $\phi_{2,\alpha}$ have been evaluated on the wing surface approximated to be at $z = 0$, t is the maximum thickness of the wing elliptic cross section, ℓ is the length of the wing, the variation of the major axis is $a = mx$, where m is the tangent of the wing leading-edge sweep angle, and the $\pm$ signs denote wing upper and lower surface, respectively. Adopting the customary approximation of thin wing theory that the pressure coefficient is given by

$$(C_p)_w = -2\phi_x \tag{24}$$

it was shown[2] that the pressures on the wing are related to those on the equivalent body by

$$(C_p)_w = (C_p)_B - \frac{mt}{2\ell}\left(1 + \ell n \frac{m\ell}{2t}\right) \mp \frac{2\alpha ma}{(a^2 - y^2)^{1/2}} \tag{25}$$

where $(C_p)_B$ represents the zero angle of attack pressure distribution on the surface of the equivalent body, a circular cone-cylinder.

In the preliminary comparisons of TER results with data for this wing,[2] results were provided only for the differences in pressures both between related points on the wing and equivalent body and also between points on the wing upper and lower surface. This was done since it was previously recognized[17] that large interference effects of the tunnel walls were present in the data that had been obtained in the Ames 2×2 ft tunnel. Consideration of the pressure differences provided an approximate means of eliminating tunnel interference from the comparisons. Prediction of the actual pressures on the equivalent body, and through application of the TER theory, on the wing were clearly unsatisfactory. In the initial comparisons of theoretical results and data for the equivalent cone-cylinder body,[17,18] considerable attention was devoted to assessing the effects of tunnel interference on the data. The analysis included a critical examination of several theoretical solutions, as well as tunnel correction procedures and additional data[13] subsequently obtained for the same body in the Ames 14-ft tunnel. Discrepancies between the experimental results, as well as among the theoretical methods, remained and were never resolved satisfactorily. It was concluded that the safer procedure to use was to rely on an evaluation of both data and theory in terms of pressure differences. We have found in this study, however, that by employing the SLOR procedure described previously for the equivalent body, the observed discrepancies can be completely accounted for. Moreover, the actual pressures observed on

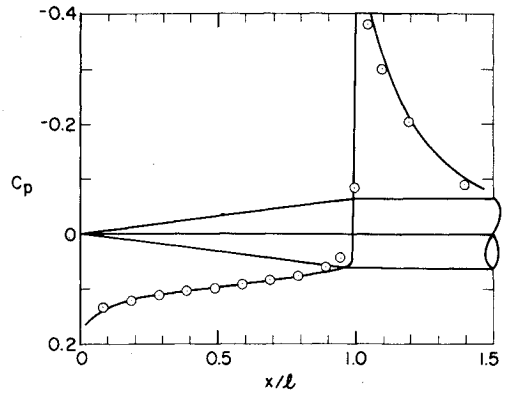

Fig. 10 Comparison of theoretical pressure distribution at $M_\infty = 1.00$ on a 7 deg semiapex angle circular cone-cylinder with data[13] obtained in a 2 × 2 ft transonic wind tunnel.

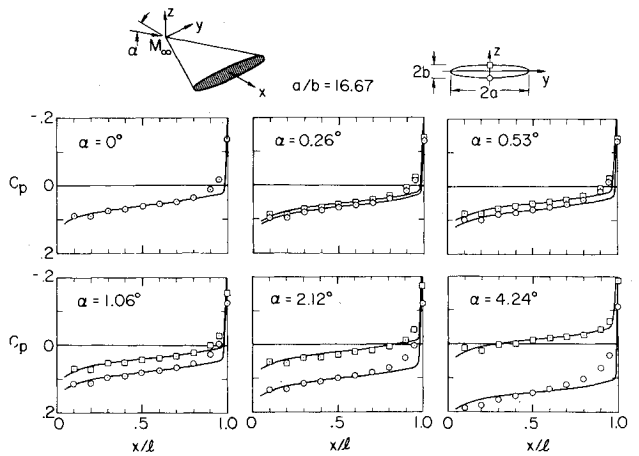

Fig. 11 Experimental[13] and TER results for surface pressures at $M_\infty = 1.00$ along the lines $\theta = (\pm 90$ deg $\square$, 0 $\circ)$ for a thin triangular wing having elliptic cross section with $a/b = 16.67$ at six angles of attack.

both the equivalent body and the triangular wing can be predicted with high accuracy. Figure 10 displays the results for the equivalent body and indicates the theoretical SLOR solution for the surface pressure on the 7 deg semiapex angle cone-cylinder at $M_\infty = 1.00$, compared with the data obtained in the Ames 2 × 2 ft transonic wind tunnel.[13] In determining these results, the homogeneous porous wall boundary condition equation (15) was employed as no flowfield data, such as reported[12] for the bodies considered in Figs. 2-9, were available for this shape. Values of the porosity from $0.2 \leq P \leq 10.0$ were used with essentially indiscernable influence on the surface pressures. The results indicated in Fig. 10 are for $P = 2.0$ and display excellent agreement with the data. Both the level and trend of the pressure are well predicted. The only discrepancy is a slight disagreement just ahead of the shoulder of the cone, apparently caused by a forward influence of the slope discontinuity at that point. These results serve both to resolve the previous discrepancies and also to provide the equivalent body ϕ_B solution for the following comparisons displayed in Fig. 11 for the triangular wing. In that figure, TER results for the surface pressures along lines on the top and bottom of the wing centerline ($y = 0$) are compared with data[13] at $M_\infty = 1.00$ for angles of attack $\alpha = 0$, 0.26, 0.53, 1.06, 2.12, and 4.24 deg. Except for a slight discrepancy in the vicinity of the shoulder of the wing ($x/\ell = 1.0$) noted previously for the equivalent body results in Fig. 10, the results are in very good agreement at all angles for which data are available.

Conclusion

An assessment of the classical transonic equivalence rule has been made by extensive comparisons of theoretical results with data for a number of three-dimensional slender shapes of aerodynamic interest. In contrast to previous comparisons, the theoretical results employ the proper equivalent body solutions based on finite-difference SLOR solutions of the axisymmetric transonic small-disturbance equation, and include the actual sting geometry of the models, as well as wind-tunnel interference effects. Particular attention was paid to tunnel interference effects by application of a novel alternative to the classical homogeneous wall condition, whereby experimentally measured flowfield pressure distributions were imposed as an outer boundary condition. Theoretical results for the axisymmetric nonlinear equivalent body flows employing this measured boundary condition exhibited highly accurate comparisons with data obtained in conventional transonic wind tunnels. Based on these equivalent body solutions, equivalence rule results for slender bodies having elliptic cross sections, at both nonlifting and lifting conditions and at Mach numbers throughout and beyond the transonic regime, display exceptionally good agreement with tunnel data. Although the classical equivalent rule locates shocks at the same longitudinal location for both the equivalent body and the actual three-dimensional configuration, a close examination of the flow in the vicinity of the embedded shocks on the surface of these shapes also exhibits good agreement, following both the trend and magnitude of the experimental results. Additional nonlifting and lifting comparisons for a thin triangular wing of unit order aspect ratio and elliptic cross section have resolved previous discrepancies associated with tunnel interference effects and exhibit good agreement with experimental results. In summary, the results presented here indicate that the classical or first-order, thickness-dominated transonic equivalence rule can provide an accurate approximation for determining transonic flow past certain three-dimensional slender configurations and the range of flow conditions and geometries over which the procedure remains effective is broad.

Acknowledgment

This research was supported by the U.S. Army Research Office under Contract DAAG29-77-C-0038.

References

[1] Spreiter, J. R. and Stahara, S. S., "Aerodynamics of Slender Bodies and Wing-Body Combinations at $M_\infty = 1$," *AIAA Journal*, Vol. 9, Sept. 1971, pp. 1784-1791.

[2] Heaslet, M. A. and Spreiter, J. R., "Three-Dimensional Transonic Flow Theory Applied to Slender Wings and Bodies," NACA Rept. 1318, 1957.

[3] Cheng, H. K. and Hafez, M. M., "Equivalence Rule and Transonic Flows Involving Lift," Dept. of Aero. Eng. Rept. USCAE 124, University of Southern California, School of Engineering, April 1973.

[4] Cheng, H. K. and Hafez, M. M., "Transonic Equivalence Rule: A Nonlinear Problem Involving Lift," *Journal of Fluid Mechanics*, Vol. 72, 1975, pp. 161-188.

[5] Oswatitsch, K., "Die theoretischen Arbeiten über schallnahe Strömungen am Flugtechnischen Institut der Kungl. Tekniska Höskolan, Stockholm," *Eighth International Congress on Theoretical and Applied Mechanics*, Istanbul, 1952, (1953), pp. 261-262.

[6] Oswatitsch, K., "The Area Rule," *Applied Mechanics Reviews*, Vol. 10, Dec. 1957, pp. 543-545.

[7] Spreiter, J. R., "Theoretical and Experimental Analysis of Transonic Flow Fields," *NACA-University Conference on Aerodynamics, Construction, and Propulsion II, "Aerodynamics,"* 1954, pp. 18-1 - 18-17.

[8] Barnwell, R. W., "Transonic Flow About Lifting Configurations," *AIAA Journal*, Vol. 11, May 1973, pp. 764-766.

[9] Bailey, F. R., "The Numerical Calculation of Transonic Flow about Slender Bodies of Revolution," NASA TN D-6582, Dec. 1971.

[10] Krupp, J. A. and Murman, E. M., "Computation of Transonic Flows Past Lifting Airfoils and Slender Bodies," *AIAA Journal*, Vol. 10, July 1972, pp. 880-886.

[11] Murman, E. M., "Analysis of Embedded Shock Waves Calculated by Relaxation Methods," *AIAA Journal*, Vol. 12, May 1974, pp. 626-633.

[12]McDevitt, J. B. and Taylor, R. A., "Force and Pressure Measurements at Transonic Speeds for Several Bodies Having Elliptical Cross Sections," NACA TN 4362, 1958.

[13]Page, W. A., "Experimental Study of the Equivalence of Transonic Flow About Slender Cone-Cylinders of Circular and Elliptic Cross Section," NACA TN 4233, 1958.

[14]Stahara, S. S. and Spreiter, J. R., "A Transonic Wind Tunnel Interference Assessment—Axisymmetric Flows," AIAA Paper 79-0203, New Orleans, La., Jan. 1979.

[15]Jameson, A., "Transonic Flow Calculations," VKI Lecture Series 87, Computational Fluid Dynamics, Von Kármán Institute for Fluid Dynamics, Rhode-St. Genesee, Belgium, March 1976.

[16]Nielsen, J. N., *Missile Aerodynamics*, McGraw-Hill Book Co., Inc., New York, 1960, p. 30.

[17]Spreiter, J. R. and Alksne, A., "Slender Body Theory Based on Approximate Solution of the Transonic Flow Equation," TR R-2, NASA, 1959.

[18]Spreiter, J. R., "Aerodynamics of Wings and Bodies at Transonic Speeds," *Journal of the Aerospace Sciences*, Vol. 26, Aug. 1959, pp. 465-487.